Available online at www.sciencedirect.com
ScienceDirect
Journal of Computational Physics 227 (2008) 4123–4141
JOURNAL OF COMPUTATIONAL PHYSICS
www.elsevier.com/locate/jcp

An unsplit Godunov method for ideal MHD via constrained transport in three dimensions

Thomas A. Gardiner [a,*], James M. Stone [a,b]

[a] Department of Astrophysical Sciences, Princeton University, Princeton, NJ 08544, United States
[b] Program in Applied and Computational Mathematics, Princeton University, Princeton, NJ 08544, United States

Received 14 September 2006; received in revised form 10 July 2007; accepted 15 December 2007
Available online 1 January 2008

Abstract

We present a single step, second-order accurate Godunov scheme for ideal MHD which is an extension of the method described in [T.A. Gardiner, J.M. Stone, An unsplit godunov method for ideal MHD via constrained transport, J. Comput. Phys. 205 (2005) 509] to three dimensions. This algorithm combines the corner transport upwind (CTU) method of Colella for multidimensional integration, and the constrained transport (CT) algorithm for preserving the divergence-free constraint on the magnetic field. We describe the calculation of the PPM interface states for 3D ideal MHD which must include multidimensional "MHD source terms" and naturally respect the balance implicit in these terms by the $\nabla \cdot \mathbf{B} = 0$ condition. We compare two different forms for the CTU integration algorithm which require either 6- or 12-solutions of the Riemann problem per cell per time-step, and present a detailed description of the 6-solve algorithm. Finally, we present solutions for test problems to demonstrate the accuracy and robustness of the algorithm.

Keywords: Magnetohydrodynamics; Numerical methods; Compressible flow

1. Introduction

In a previous paper [1], we described a two-dimensional (2D), second-order accurate Godunov method for ideal MHD that evolves the magnetic field using the constrained transport (CT) [11] algorithm for preserving the divergence-free constraint on the magnetic field. In its simplest form, CT requires area-averaged values of the magnetic field which are stored at cell faces. We argued that this is the most natural discrete representation of the field in that the integral form of the induction equation is based on area (rather than volume) averages, and therefore, the discrete form of the equations should respect this difference. There are three important ingredients to our MHD algorithm: (1) a modification of the piecewise parabolic method (PPM) [8] reconstruction step used to construct time-advanced estimates of the conserved variables on cell faces that are fed to the Riemann solver to incorporate multidimensional terms essential in MHD, (2) a new method for con-

* Corresponding author. Tel.: +1 609 575 3055.
E-mail address: gardiner@astro.princeton.edu (T.A. Gardiner).

0021-9991/$ - see front matter © 2007 Elsevier Inc. All rights reserved.
doi:10.1016/j.jcp.2007.12.017

structing the fluxes (at cell edges) of the area-averaged magnetic fields (at cell faces) from the fluxes returned by the Riemann solver (at cell faces) of volume-averaged magnetic fields (at cell centers) which are based on the fundamental relationship between the area- and volume-averaged variables, and (3) a directionally unsplit integration algorithm based on the corner transport upwind (CTU) method [7].

Through a series of test problems (in particular, the advection of 2D field loops) we showed that our new methods for constructing the fluxes needed by the CT algorithm are essential for stability. Moreover, by using the second-order accurate CTU integration algorithm, we showed a method could be constructed which has less numerical dissipation and has the important property of reducing exactly to the one-dimensional (1D) algorithm for plane-parallel, grid-aligned flows. Since CT does not require costly solutions to elliptic equations, we expect MHD Godunov schemes based on CT to be more cost effective that those that use divergence-cleaning [9,19]. Given the attractive properties of the method, it is of interest to extend it to three-dimensions (3D) for use in applications.

When directional splitting is used, the extension of Godunov methods from 2D to 3D is usually trivial. However, directional splitting is unsuitable for MHD, because it is impossible to enforce the divergence-free constraint between partial updates unless all three components of the magnetic field are updated together, which in turn violates the assumption basic to splitting that each dimensional operator is independent and can be split from the others. As a result, in [1] we adopted the unsplit CTU integration scheme. Even in hydrodynamics, the extension of CTU to 3D is not trivial [17]. For our MHD algorithm, extension to 3D requires modifying two of the three ingredients of the method, in particular (1) the PPM reconstruction algorithm must be modified to include multidimensional terms for MHD in such a way as to respect a *balance* law implied by the $\nabla \cdot \mathbf{B} = 0$ condition, and (2) the CTU algorithm must be modified to include source terms as well as the transverse flux gradient terms. The primary purpose of this paper is to describe in detail these modifications and to demonstrate that the resulting algorithm is both accurate and robust.

We extend our MHD test suite to 3D to demonstrate the accuracy and fidelity of our method. We find that, once again, the passive advection of a multidimensional field loop is a challenging test of finite volume methods for MHD. In particular, for a field loop confined to the (x, y)-plane in 3D advected with a constant velocity with $v_z \neq 0$, the vertical component of the magnetic field B_z will evolve unless care is made to ensure the multidimensional balance of MHD source terms in both the PPM characteristic tracing step and the transverse flux gradient update step. In fact, this observation leads to a useful definition of the appropriate difference stencil on which the divergence-free constraint must be maintained. If $\nabla \cdot \mathbf{B} = 0$ on a stencil which is different from that used to construct the fluxes of B_z, the latter will show unphysical evolution in this test for conservative algorithms. For the same reason, if a numerical method keeps B_z constant to round-off error on the test, it must preserve the divergence-free constraint on the appropriate stencil. Moreover, this test is another demonstration that it is *essential* to maintain the divergence-free constraint *exactly* in MHD, as was originally emphasized by [6]. This test, along with several others are presented in Section 6.

The paper is organized as follows. In Section 2, we write down the equations of ideal MHD solved by our method. In Section 3, we describe our extension of the PPM reconstruction algorithm to 3D MHD. In Section 4 we describe two formulations for the CTU integration algorithm in 3D, in Section 5 we present results from a 3D test suite, and in Section 6 we conclude.

2. Ideal magnetohydrodynamics and constrained transport

The equations of ideal magnetohydrodynamics (MHD) can be written in conservative form as

$$\frac{\partial \rho}{\partial t} + \nabla \cdot (\rho \mathbf{v}) = 0, \tag{1}$$

$$\frac{\partial \rho \mathbf{v}}{\partial t} + \nabla \cdot (\rho \mathbf{v}\mathbf{v} - \mathbf{B}\mathbf{B}) + \nabla P^* = 0, \tag{2}$$

$$\frac{\partial \mathbf{B}}{\partial t} + \nabla \times (\mathbf{B} \times \mathbf{v}) = 0, \tag{3}$$

$$\frac{\partial E}{\partial t} + \nabla \cdot ((E + P^*)\mathbf{v} - \mathbf{B}(\mathbf{B} \cdot \mathbf{v})) = 0, \tag{4}$$

where ρ is the mass density, $\rho\mathbf{v}$ the momentum density, $\mathbf{B}$ the magnetic field, and E the total energy density. The total pressure $P^* \equiv P + (\mathbf{B}\cdot\mathbf{B})/2$ where P is the gas pressure. This system of equations is closed with the addition of an equation of state which relates the pressure and density to the internal energy:

$$\epsilon \equiv E - \rho(\mathbf{v}\cdot\mathbf{v})/2 - (\mathbf{B}\cdot\mathbf{B})/2. \tag{5}$$

Throughout this paper, we will assume an ideal gas equation of state for which $P = (\gamma - 1)\epsilon$, where γ is the ratio of specific heats. Note that we have chosen a system of units in which the magnetic permeability $\mu = 1$.

In this paper, we will assume a regular, 3D, Cartesian grid. We will use the standard notation that grid cell (i, j, k) is centered at (x_i, y_j, z_k) and has a size $(\delta x, \delta y, \delta z)$. Time levels will be denoted by a superscript and interface values will be denoted by half increments to the index, e.g. the volume-averaged x-component of the magnetic field at time t^n is defined to be

$$B^n_{x,i,j,k} \equiv \frac{1}{2}\left(B^n_{x,i-1/2,j,k} + B^n_{x,i+1/2,j,k}\right). \tag{6}$$

3. Calculating the interface states

The PPM interface state algorithm is based upon the idea of dimensional splitting, and as a result it is a 1D algorithm including both spatial reconstruction and a characteristic evolution of the linearized system in primitive variables. For ideal MHD, however, it was shown in [1] that it is necessary to include multidimensional terms when calculating the interface states. The 3D interface state algorithm is thus a generalization of the 2D algorithm which for consistency must reduce to the 2D and 1D algorithm in the appropriate limits. The interface states in the PPM algorithm are typically calculated by evolving the system of equations in primitive variables. Consider the induction equation (4) for the z-component of the magnetic field

$$\frac{\partial B_z}{\partial t} + \frac{\partial}{\partial x}(v_x B_z - B_x v_z) + \frac{\partial}{\partial y}(v_y B_z - B_y v_z) = 0. \tag{7}$$

The terms proportional to $\partial B_x/\partial x$ and $\partial B_y/\partial y$ (and those proportional to $\partial B_z/\partial z$ in the equations for the other two components) we refer to as "MHD source terms". (When the system of equations for MHD is written in primitive variables, these source terms only appear in the induction equation. As a result we will not discuss the remaining MHD equations in this section.) The question before us is: which terms in the induction equation need to be included in the calculation of the interface states? In what follows we specialize to the calculation of the x-interface states; the y- and z-interface state calculation follows by symmetry.

3.1. 3D MHD interface state algorithm

A comprehensive description of the 2D MHD interface state algorithm is provided in Section 3.1 of [1]. The most important point to note here is that the *balance* of the MHD source terms resulting from the $\nabla\cdot\mathbf{B} = 0$ condition must be accurately represented in the calculation of the interface states. The 3D interface algorithm is constructed explicitly to incorporate the potential balance between the MHD source terms and to reduce exactly to the 2D interface states algorithm in the limit that the problems is 2D and grid-aligned. The essential idea is to rewrite the induction equation as follows prior to applying the idea of directional splitting:

$$\frac{\partial B_x}{\partial t} + \left\{\frac{\partial}{\partial y}(v_y B_x - B_y v_x) - v_x L_{xy}\left(\frac{\partial B_z}{\partial z}\right)\right\} + \left\{\frac{\partial}{\partial z}(v_z B_x - B_z v_x) - v_x L_{xz}\left(\frac{\partial B_y}{\partial y}\right)\right\} = 0, \tag{8}$$

$$\frac{\partial B_y}{\partial t} + \left\{\frac{\partial}{\partial x}(v_x B_y - B_x v_y) - v_y L_{yx}\left(\frac{\partial B_z}{\partial z}\right)\right\} + \left\{\frac{\partial}{\partial z}(v_z B_y - B_z v_y) - v_y L_{yz}\left(\frac{\partial B_x}{\partial x}\right)\right\} = 0, \tag{9}$$

$$\frac{\partial B_z}{\partial t} + \left\{\frac{\partial}{\partial x}(v_x B_z - B_x v_z) - v_z L_{zx}\left(\frac{\partial B_y}{\partial y}\right)\right\} + \left\{\frac{\partial}{\partial y}(v_y B_z - B_y v_z) - v_z L_{zy}\left(\frac{\partial B_x}{\partial x}\right)\right\} = 0, \tag{10}$$

where we have added a limited amount of the transverse MHD source term to each component of the electric field gradient and grouped terms according to the fashion in which they will be split. The mathematical form

of the limiter functions, e.g. L_{xy}, is determined by imposing constraints on the directionally split and unsplit system. Clearly, to recover the induction equation we have

$$L_{xy}\left(\frac{\partial B_z}{\partial z}\right) = -L_{xz}\left(\frac{\partial B_y}{\partial y}\right), \tag{11}$$

etc. Directionally split, we obtain the following system for the x-coordinate direction:

$$\frac{\partial B_x}{\partial t} = 0, \tag{12}$$

$$\frac{\partial B_y}{\partial t} + \frac{\partial}{\partial x}(v_x B_y - B_x v_y) - v_y L_{yx}\left(\frac{\partial B_z}{\partial z}\right) = 0, \tag{13}$$

$$\frac{\partial B_z}{\partial t} + \frac{\partial}{\partial x}(v_x B_z - B_x v_z) - v_z L_{zx}\left(\frac{\partial B_y}{\partial y}\right) = 0. \tag{14}$$

To determine the form of the limiter functions, we minimize the magnitude of the sum of the MHD source terms. For Eq. (14) we find

$$L_{zx}\left(\frac{\partial B_y}{\partial y}\right) = \operatorname{minmod}\left(-\frac{\partial B_x}{\partial x}, \frac{\partial B_y}{\partial y}\right), \tag{15}$$

where the minmod function is defined as

$$\operatorname{minmod}(x,y) = \begin{cases} \operatorname{sign}(x)\min(|x|,|y|) & \text{if } xy > 0, \\ 0 & \text{otherwise.} \end{cases} \tag{16}$$

Note that this limiter function satisfies the constraint identified in Eq. (11). The mathematical form of the remaining limiter functions in Eqs. (8)–(10) is given by cyclic permutation of (x,y,z) in Eq. (15) and application of the constraint noted in Eq. (11).

There is also a simple physical argument for why the limiter function takes the form described by Eq. (15). Considering Eq. (7), if $(\partial B_x/\partial x)$ and $(\partial B_y/\partial y)$ have opposite signs, but not necessarily the same magnitude we wish to incorporate the balance of these two MHD source terms by adding and subtracting the term with the smaller magnitude so that the resulting (reduced) MHD source term is associated with only one of the flux gradients. If, on the other hand, these derivatives have the same sign, then there is no balance between the source terms and the induction equation should be unmodified. This is precisely the result of the minmod limited source term in Eq. (15).

Finally, we note that using the properties of the minmod function and the $\nabla \cdot \mathbf{B} = 0$ condition, Eqs. (12)–(14) can be simplified to

$$\frac{\partial B_x}{\partial t} = 0, \tag{17}$$

$$\frac{\partial B_y}{\partial t} + \frac{\partial}{\partial x}(v_x B_y) - B_x \frac{\partial v_y}{\partial x} - v_y \operatorname{minmod}\left(\frac{\partial B_x}{\partial x}, -\frac{\partial B_y}{\partial y}\right) = 0, \tag{18}$$

$$\frac{\partial B_z}{\partial t} + \frac{\partial}{\partial x}(v_x B_z) - B_x \frac{\partial v_z}{\partial x} - v_z \operatorname{minmod}\left(\frac{\partial B_x}{\partial x}, -\frac{\partial B_z}{\partial z}\right) = 0 \tag{19}$$

for calculating the x-interface states. As a practical matter, these limited MHD source terms are evaluated in terms of the cell average of the magnetic field gradients, i.e. for Eq. (19) in cell (i,j,k) we use

$$\operatorname{minmod}\left(\frac{B_{x,i+1/2,j,k} - B_{x,i-1/2,j,k}}{\delta x}, \frac{B_{z,i,j,k-1/2} - B_{x,i,j,k+1/2}}{\delta z}\right). \tag{20}$$

The equations for the y- and z-interface states follow from cyclic permutations of (x,y,z). In the limiting 2D case of either $\partial/\partial y = 0$ or $\partial/\partial z = 0$ this approach reduces to the interface state algorithm outlined in [1]. Moreover, in the limiting 2D case of $\partial/\partial x = 0$, the x-interface state will equal the cell center state, just what one expects from 1D and 2D calculations.

4. Corner transport upwind algorithm

The CTU algorithm originally described by Colella [7] is an unsplit, 2D finite volume algorithm for solving hyperbolic systems of conservation laws. The 3D generalization of the CTU algorithm was subsequently presented by Saltzman [17]. In this section, we present two variants of the 3D CTU integration algorithm. In Section 4.1, we present a brief, functional description of the algorithm described by Saltzman [17] which we refer to here as the 12-solve algorithm since it requires 12 solutions to the Riemann problem per zone per time-step. However, because of its complexity, we will not present the algorithmic elements for the 12-solve MHD CTU algorithm in detail. In Section 4.2, we present a simple variant which requires only 6 solutions to the Riemann problem per zone per time-step and describe this 6-solve algorithm in detail. We summarize with a discussion of the strengths and weaknesses of this algorithm relative to the 12-solve CTU algorithm as a prelude to Section 5 where we present a variety of results for both.

For both the 6-solve and 12-solve algorithms, an algorithm for constructing the grid cell edge averaged electric fields from the Godunov fluxes is needed. This algorithm is typically referred to as a CT algorithm. It can be described as a predictor/corrector process where the Godunov electric fields are the predictor values and the resulting CT electric fields are the corrector values. In [1], a simple framework for constructing CT algorithms was presented and a few CT algorithms were constructed and tested. In this paper, we adopt the $\mathcal{E}^c$ CT algorithm defined by Eqs. (41) and (50) in [1], as it was shown to have the best properties. The $\mathcal{E}^c$ CT algorithm is constructed in such a way as contain an upwind bias (according to the contact mode) and to reduce to the correct Godunov EMF for grid-aligned, plane-parallel flows. Details of the algorithm is given in [1] and will not be repeated here.

4.1. 12-Solve CTU

We begin by choosing a numerical flux function $\mathcal{F}(q_{\rm L}, q_{\rm R})$ which is assumed to return a suitably accurate solution for the flux obtained by solving the Riemann problem associated with $q_{\rm L}$ and $q_{\rm R}$, the left and right states. The 12-solve CTU algorithm can then be described as follows (see [7,14,17]).

Step 1, calculate the left and right PPM interface states $q^*_{{\rm L}x,i+1/2,j,k}, q^*_{{\rm R}x,i+1/2,j,k}$ and the associated interface flux

$$F^*_{x,i+1/2,j,k} = \mathcal{F}_x(q^*_{{\rm L}x,i+1/2,j,k}, q^*_{{\rm R}x,i+1/2,j,k}) \tag{21}$$

with similar expressions for the y- and z-direction fluxes.

Step 2, for each interface state calculate two interface states evolved by $\delta t/3$ of a single transverse flux gradient, i.e.

$$q^{*|y}_{{\rm L}x,i+1/2,j,k} = q^*_{{\rm L}x,i+1/2,j,k} + \frac{\delta t}{3\,\delta y}(F^*_{y,i,j-1/2,k} - F^*_{y,i,j+1/2,k}), \tag{22}$$

$$q^{*|y}_{{\rm R}x,i+1/2,j,k} = q^*_{{\rm R}x,i+1/2,j,k} + \frac{\delta t}{3\,\delta y}(F^*_{y,i+1,j-1/2,k} - F^*_{y,i+1,j+1/2,k}), \tag{23}$$

$$q^{*|z}_{{\rm L}x,i+1/2,j,k} = q^*_{{\rm L}x,i+1/2,j,k} + \frac{\delta t}{3\,\delta z}(F^*_{z,i,j,k-1/2} - F^*_{z,i,j,k+1/2}), \tag{24}$$

$$q^{*|z}_{{\rm R}x,i+1/2,j,k} = q^*_{{\rm R}x,i+1/2,j,k} + \frac{\delta t}{3\,\delta z}(F^*_{z,i+1,j,k-1/2} - F^*_{z,i+1,j,k+1/2}) \tag{25}$$

with y- and z-interface states being defined in an equivalent manner by cyclic permutation of (x,y,z) and (i,j,k). For each of the $\delta t/3$ updated interface states, calculate the associated flux, giving the two x-interface fluxes

$$F^{*|y}_{x,i+1/2,j,k} = \mathcal{F}_x\left(q^{*|y}_{{\rm L}x,i+1/2,j,k}, q^{*|y}_{{\rm R}x,i+1/2,j,k}\right), \tag{26}$$

$$F^{*|z}_{x,i+1/2,j,k} = \mathcal{F}_x\left(q^{*|z}_{{\rm L}x,i+1/2,j,k}, q^{*|z}_{{\rm R}x,i+1/2,j,k}\right) \tag{27}$$

and similar expressions for the y- and z-interface fluxes.

Step 3, at each interface evolve the PPM interface states by $\delta t/2$ of the transverse flux gradients, i.e.

$$q^{n+1/2}_{\mathrm{L}x,i+1/2,j,k} = q^{*}_{\mathrm{L}x,i+1/2,j,k} + \frac{\delta t}{2\delta y}\left(F^{*|z}_{y,i,j-1/2,k} - F^{*|z}_{y,i,j+1/2,k}\right) \tag{28}$$

$$+ \frac{\delta t}{2\,\delta z}\left(F^{*|y}_{z,i,j,k-1/2} - F^{*|y}_{z,i,j,k+1/2}\right), \tag{29}$$

$$q^{n+1/2}_{\mathrm{R}x,i+1/2,j,k} = q^{*}_{\mathrm{R}x,i+1/2,j,k} + \frac{\delta t}{2\delta y}\left(F^{*|z}_{y,i+1,j-1/2,k} - F^{*|z}_{y,i+1,j+1/2,k}\right) \tag{30}$$

$$+ \frac{\delta t}{2\,\delta z}\left(F^{*|y}_{z,i+1,j,k-1/2} - F^{*|y}_{z,i+1,j,k+1/2}\right) \tag{31}$$

with y- and z-interface states being defined in an equivalent manner by cyclic permutation of (x,y,z) and (i,j,k). For each of the $\delta t/2$ updated interface states, calculate the associated flux, giving the x-interface flux

$$F^{n+1/2}_{x,i+1/2,j,k} = \mathcal{F}_x\left(q^{n+1/2}_{\mathrm{L}x,i+1/2,j,k}, q^{n+1/2}_{\mathrm{R}x,i+1/2,j,k}\right) \tag{32}$$

and similar expressions for the y- and z-interface fluxes.

Step 4, update the conserved variables from time n to $n+1$ via the fully corner coupled numerical fluxes

$$q^{n+1}_{i,j,k} = q^{n}_{i,j,k} + \frac{\delta t}{\delta x}\left(F^{n+1/2}_{x,i-1/2,j,k} - F^{n+1/2}_{x,i+1/2,j,k}\right) \tag{33}$$

$$+ \frac{\delta t}{\delta y}\left(F^{n+1/2}_{y,i,j-1/2,k} - F^{n+1/2}_{y,i,j+1/2,k}\right) + \frac{\delta t}{\delta z}\left(F^{n+1/2}_{z,i,j,k-1/2} - F^{n+1/2}_{z,i,j,k+1/2}\right). \tag{34}$$

This completes the description of the 12-solve CTU algorithm for a typical system of conservation laws, such as Euler's equations. Unfortunately, as written above, the 12-solve CTU algorithm does not result in a useful method for ideal MHD. This can be understood on rather general grounds by noting that the intermediate steps in the algorithm use partial updates based on a dimensional splitting of the equations in conservation form. This in turn ignores the potential balance between flux gradients in different directions (in particular MHD source terms associated with those flux gradients) which is always present for MHD owing to the $\nabla \cdot \mathbf{B} = 0$ constraint.

To make this point more concrete, note that the parallel flux gradient terms (x-flux gradient at x-interfaces, etc.) are included in the PPM interface states algorithm using the dimensionally split, primitive form of the equations for MHD. Meanwhile, the transverse flux gradient terms are included using the conservative form of the equations. Since the dimensionally split primitive and conservative form of the equations for MHD are not commensurate, this amounts to neglecting certain MHD source terms resulting in a formally first-order accurate integration algorithm. In addition, such an algorithm would also show secular evolution of a magnetic field component perpendicular to the magnetic field loop in the *gedanken* experiment discussed in [1] and Section 1.

For the 3D 12-solve CTU algorithm, with two predictor steps, the source term correction procedure required to provide balance to the flux gradient terms is increasingly complicated. The advantage of 12-solve CTU algorithm is that it is optimally stable for CFL numbers $\leqslant 1$. The disadvantage is that the algorithm is complicated. We have implemented the 12-solve MHD CTU algorithm as described above and present results of tests of the method in Section 5. However, the complexity of the method motivates us to find a simpler alternative, which we describe below.

4.2. 6-Solve CTU variant for MHD

For Euler's equations, the 6-solve algorithm can be described concisely as the 12-solve CTU algorithm of Section 4.1 omitting step 2 and replacing $F^{*|y}_{x,i+1/2,j,k}$ and $F^{*|z}_{x,i+1/2,j,k}$ with $F^{*}_{x,i+1/2,j,k}$ (and similarly for the y- and z-fluxes) in step 3. Alternatively, one may also describe it as a formal extension of the 2D CTU algorithm in which the parallel and transverse flux gradients are included in the interface states in a two-step process. The algorithm consists of the following steps.

Step 1, calculate the left and right PPM interface states $q^*_{\mathrm{L}x,i+1/2,j,k}$ and $q^*_{\mathrm{R}x,i+1/2,j,k}$ including the MHD source terms described in Section 3.1 and the associated interface flux

$$F^*_{x,i+1/2,j,k} = \mathcal{F}_x(q^*_{\mathrm{L}x,i+1/2,j,k}, q^*_{\mathrm{R}x,i+1/2,j,k}) \tag{35}$$

with similar expressions for the y- and z-direction fluxes.

Step 2, apply the CT algorithm of [1] to calculate the CT electric fields $\mathcal{E}^*_{x,i,j+1/2,k+1/2}, \mathcal{E}^*_{y,i+1/2,j,k+1/2}$ and $\mathcal{E}^*_{z,i+1/2,j+1/2,k}$ using the numerical fluxes from step 1 and a cell center reference electric field calculated using the initial data at time level n, i.e. $q^n_{i,j,k}$.

Step 3, at each interface evolve the PPM interface states by $\delta t/2$ of the transverse flux gradients. The hydrodynamic variables (mass, momentum and energy density) are advanced using

$$q^{n+1/2}_{\mathrm{L}x,i+1/2,j,k} = q^*_{\mathrm{L}x,i+1/2,j,k} + \frac{\delta t}{2\,\delta y}(F^*_{y,i,j-1/2,k} - F^*_{y,i,j+1/2,k}) + \frac{\delta t}{2\,\delta z}(F^*_{z,i,j,k-1/2} - F^*_{z,i,j,k+1/2}) + \frac{\delta t}{2} S_{x,i,j,k}, \tag{36}$$

$$q^{n+1/2}_{\mathrm{R}x,i+1/2,j,k} = q^*_{\mathrm{R}x,i+1/2,j,k} + \frac{\delta t}{2\,\delta y}(F^*_{y,i+1,j-1/2,k} - F^*_{y,i+1,j+1/2,k}) + \frac{\delta t}{2\,\delta z}(F^*_{z,i+1,j,k-1/2} - F^*_{z,i+1,j,k+1/2}) + \frac{\delta t}{2} S_{x,i+1,j,k}, \tag{37}$$

where the x-interface MHD source term for the momentum density

$$(S_{x,i,j,k})_{\rho\mathbf{v}} = \mathbf{B}_{i,j,k}\left(\frac{\partial B_x}{\partial x}\right)_{i,j,k} \tag{38}$$

and the energy density

$$(S_{x,i,j,k})_E (B_y v_y)_{i,j,k} \mathrm{minmod}\left(-\frac{\partial B_z}{\partial z}, \frac{\partial B_x}{\partial x}\right)_{i,j,k} + (B_z v_z)_{i,j,k} \mathrm{minmod}\left(-\frac{\partial B_y}{\partial y}, \frac{\partial B_x}{\partial x}\right)_{i,j,k}. \tag{39}$$

The magnetic field components are evolved using the CT electric fields in place of the predictor fluxes. The interface normal component of the magnetic field is evolved using the integral form of the Stokes loop:

$$B^{n+1/2}_{x,i+1/2,j,k} B^n_{x,i+1/2,j,k} - \frac{\delta t}{2\,\delta y}(\mathcal{E}^*_{z,i+1/2,j+1/2,k} - \mathcal{E}^*_{z,i+1/2,j-1/2,k}) + \frac{\delta t}{2\,\delta z}(\mathcal{E}^*_{y,i+1/2,j,k+1/2} - \mathcal{E}^*_{y,i+1/2,j,k-1/2}). \tag{40}$$

The y-component of the magnetic field is evolved using

$$\begin{aligned}(B_y)^{n+1/2}_{\mathrm{L}x,i+1/2,j,k} = (B_y)^*_{\mathrm{L}x,i+1/2,j,k} &- \frac{\delta t}{4\,\delta z}(\mathcal{E}^*_{x,i,j+1/2,k+1/2} - \mathcal{E}^*_{x,i,j+1/2,k-1/2}) \\ &- \frac{\delta t}{4\,\delta z}(\mathcal{E}^*_{x,i,j-1/2,k+1/2} - \mathcal{E}^*_{x,i,j-1/2,k-1/2}) + \frac{\delta t}{2}(S_{x,i,j,k})_{B_y},\end{aligned} \tag{41}$$

$$\begin{aligned}(B_y)^{n+1/2}_{\mathrm{R}x,i+1/2,j,k} = (B_y)^*_{\mathrm{R}x,i+1/2,j,k} &- \frac{\delta t}{4\,\delta z}(\mathcal{E}^*_{x,i+1,j+1/2,k+1/2} - \mathcal{E}^*_{x,i+1,j+1/2,k-1/2}) \\ &- \frac{\delta t}{4\,\delta z}(\mathcal{E}^*_{x,i+1,j-1/2,k+1/2} - \mathcal{E}^*_{x,i+1,j-1/2,k-1/2}) + \frac{\delta t}{2}(S_{x,i+1,j,k})_{B_y}\end{aligned} \tag{42}$$

with

$$(S_{x,i,j,k})_{B_y} = (v_y)_{i,j,k} \mathrm{minmod}\left(-\frac{\partial B_z}{\partial z}, \frac{\partial B_x}{\partial x}\right)_{i,j,k}. \tag{43}$$

The z-component of the magnetic field is evolved using

$$\begin{aligned}(B_z)^{n+1/2}_{\mathrm{L}x,i+1/2,j,k} = (B_z)^*_{\mathrm{L}x,i+1/2,j,k} &+ \frac{\delta t}{4\,\delta y}(\mathcal{E}^*_{x,i,j+1/2,k+1/2} - \mathcal{E}^*_{x,i,j-1/2,k+1/2}) \\ &+ \frac{\delta t}{4\,\delta y}(\mathcal{E}^*_{x,i,j+1/2,k-1/2} - \mathcal{E}^*_{x,i,j-1/2,k-1/2}) + \frac{\delta t}{2}(S_{x,i,j,k})_{B_z},\end{aligned} \tag{44}$$

$$(B_z)^{n+1/2}_{\mathrm{R}x,i+1/2,j,k} = (B_z)^{*}_{\mathrm{R}x,i+1/2,j,k} + \frac{\delta t}{4\,\delta y}(\mathcal{E}^{*}_{x,i+1,j+1/2,k+1/2} - \mathcal{E}^{*}_{x,i+1,j-1/2,k+1/2}) + \frac{\delta t}{4\,\delta y}(\mathcal{E}^{*}_{x,i+1,j+1/2,k-1/2} - \mathcal{E}^{*}_{x,i+1,j-1/2,k-1/2}) + \frac{\delta t}{2}(S_{x,i+1,j,k})_{B_z} \tag{45}$$

with

$$(S_{x,i,j,k})_{B_z} = (v_z)_{i,j,k}\mathrm{minmod}\left(-\frac{\partial B_y}{\partial y}, \frac{\partial B_x}{\partial x}\right)_{i,j,k}. \tag{46}$$

Note that the origin of these MHD source terms for the transverse components of the magnetic field can be clearly seen as resulting from the directional splitting of the induction equation described in Section 3.1. The momentum and energy density MHD source terms originate from the use of the primitive variable form of the MHD equations to calculate the PPM interface states. The y- and z-interface states are advanced in an equivalent manner by cyclic permutation of (x, y, z) and (i, j, k) in the above expressions.

Step 4, for each of the $\delta t/2$ updated interface states, calculate the associated flux, giving the x-interface flux

$$F^{n+1/2}_{x,i+1/2,j,k} = \mathcal{F}_x\left(q^{n+1/2}_{\mathrm{L}x,i+1/2,j,k}, q^{n+1/2}_{\mathrm{R}x,i+1/2,j,k}\right) \tag{47}$$

and similar expressions for the y- and z-interface fluxes.

Step 5, apply the CT algorithm of [1] to calculate the CT electric fields $\mathcal{E}^{n+1/2}_{x,i,j+1/2,k+1/2}$, $\mathcal{E}^{n+1/2}_{y,i+1/2,j,k+1/2}$ and $\mathcal{E}^{n+1/2}_{z,i+1/2,j+1/2,k}$ using the numerical fluxes from step 4 and a cell center reference electric field calculated using the cell average state at time level $n + 1/2$ which is calculated as follows. The cell center magnetic field components are defined as equaling the arithmetic average of the interface magnetic field components, $B^{n+1/2}_{x,i,j,k} = (B^{n+1/2}_{x,i+1/2,j,k} + B^{n+1/2}_{x,i-1/2,j,k})/2$ and similarly for the y- and z-components. The mass and momentum density are computed using a conservative update with the predictor fluxes from step 1

$$q^{n+1/2}_{i,j,k} = q^{n}_{i,j,k} + \frac{\delta t}{2\,\delta x}(F^{*}_{x,i-1/2,j,k} - F^{*}_{x,i+1/2,j,k}) + \frac{\delta t}{2\,\delta y}(F^{*}_{y,i,j-1/2,k} - F^{*}_{y,i,j+1/2,k}) + \frac{\delta t}{2\,\delta z}(F^{*}_{z,i,j,k-1/2} - F^{*}_{z,i,j,k+1/2}). \tag{48}$$

Step 6, update the solution from time level n to $n + 1$. The hydrodynamic variables (mass, momentum and energy density) are advanced using the standard the flux integral relation:

$$q^{n+1}_{i,j,k} = q^{n}_{i,j,k} + \frac{\delta t}{\delta x}\left(F^{n+1/2}_{x,i-1/2,j,k} - F^{n+1/2}_{x,i+1/2,j,k}\right) + \frac{\delta t}{\delta y}\left(F^{n+1/2}_{y,i,j-1/2,k} - F^{n+1/2}_{y,i,j+1/2,k}\right) + \frac{\delta t}{\delta z}\left(F^{n+1/2}_{z,i,j,k-1/2} - F^{n+1/2}_{z,i,j,k+1/2}\right) \tag{49}$$

and the interface averaged normal components of the magnetic field are advanced using a Stokes loop integral, for example the x-component of the equation is

$$B^{n+1}_{x,i+1/2,j,k} = B^{n}_{x,i+1/2,j,k} - \frac{\delta t}{\delta y}\left(\mathcal{E}^{n+1/2}_{z,i+1/2,j+1/2,k} - \mathcal{E}^{n+1/2}_{z,i+1/2,j-1/2,k}\right) + \frac{\delta t}{\delta z}\left(\mathcal{E}^{n+1/2}_{y,i+1/2,j,k+1/2} - \mathcal{E}^{n+1/2}_{y,i+1/2,j,k-1/2}\right) \tag{50}$$

with similar expressions for the y- and z-components.

This completes the description of the 6-solve CTU algorithm. This relatively simple 3D integration algorithm is second-order accurate and has the advantage over the 12-solve CTU algorithm that no source terms need be included in the evolution of the interface normal components of the magnetic field. This algorithm is designed in such a way that for grid-aligned flows it reduces exactly to the 2D CTU and 1D PPM integration algorithms for problems involving the relevant symmetry. The downside is that we observe experimentally that the algorithm is stable for CFL $< 1/2$. Hence, to a large extent the 6-solve and 12-solve algorithms show similar computational cost: two time-steps with the 6-solve algorithm at a CFL number of 1/2 is nearly equivalent to one time-step with the 12-solve algorithm with a CFL number of one.

5. Tests

In this section, we present and compare results obtained with both the 6-solve and 12-solve CTU + CT integration algorithm just described.

5.1. Field loop advection

The advection of a weak magnetic field loop, a problem studied in [1], is a surprisingly difficult test for conservative finite volume methods applied to the ideal MHD equations. In particular, consider a field loop confined to the (x,y)-plane, i.e. $B_z = 0$, and a constant advection velocity field with $v_z \neq 0$. If care is not taken to respect the balance between the MHD source terms in calculating the interface states, updating them with transverse flux gradients, etc. one can find an erroneous and sometimes *secular* evolution of B_z. In fact any scheme which is conservative but does not satisfy $\nabla \cdot \mathbf{B} = 0$ will find erroneous evolution for B_z in this problem. Similarly if a conservative numerical algorithm can solve this magnetic field loop advection problem and preserve the solution $B_z = 0$ for all time, it also satisfies the $\nabla \cdot \mathbf{B} = 0$ condition.

The test consists of a computational domain $-0.5 \leqslant x \leqslant 0.5$, $-0.5 \leqslant y \leqslant 0.5$, and $-1 \leqslant z \leqslant 1$, resolved on a $N \times N \times 2N$ grid with periodic boundary conditions. The hydrodynamical state is uniform with a density $\rho = 1$, pressure $P = 1$, and velocity components $(v_x, v_y, v_z) = (1, 1, 2)$. The initialization of the magnetic field is most easily described in terms of a vector potential in the coordinate system (x_1, x_2, x_3) which is related to the computational coordinate system (x, y, z) via the rotation

$$\begin{aligned} x_1 &= (2x + z)/\sqrt{5}, \\ x_2 &= y, \\ x_3 &= (-x + 2z)/\sqrt{5}. \end{aligned} \tag{51}$$

In particular, we choose $A_1 = A_2 = 0$ and

$$A_3 = \begin{cases} B_0(R - r) & \text{for } r \leqslant R, \\ 0 & \text{for } r > R, \end{cases} \tag{52}$$

where $B_0 = 10^{-3}, R = 0.3$ and $r = \sqrt{x_1^2 + x_2^2}$ in the domain $-0.5\lambda_1 \leqslant x_1 \leqslant 0.5\lambda_1$, $-0.5\lambda_2 \leqslant x_2 \leqslant 0.5\lambda_2$. To satisfy the periodic boundary conditions we choose $\lambda_1 = 2/\sqrt{5}$ and $\lambda_2 = 1$ and define $A_3(x_1 + n\lambda_1, x_2 + m\lambda_2, x_3) = A_3(x_1, x_2, x_3)$ for all integers (n, m).

The time evolution of the volume-averaged magnetic energy density $\langle B^2 \rangle$ normalized to the initial (analytic) value $\langle B^2 \rangle = \left(\sqrt{5}\pi R^2/2\right) B_0^2$ is plotted in Fig. 1. The magnetic energy density $\langle B^2 \rangle$ can be well fit as a power law of the form $\langle B^2 \rangle = C(1 - (t/\tau)^\alpha)$ where $\tau = (3.22 \times 10^2, 3.68 \times 10^3, 2.65 \times 10^4)$ and $\alpha = (0.365, 0.328, 0.320)$ for $N = (32, 64, 128)$, respectively. These values are quite comparable to the time constant $\tau = 1.061 \times 10^4$ and exponent $\alpha = 0.291$ found in the 2D calculation.

For the specific case of a cylindrical magnetic field loop with translation invariance in the z-direction $(\partial/\partial z = 0)$ the 6-solve and 12-solve algorithms studied in this paper reduce exactly to the 2D algorithm presented in [1]. As such, the 3D algorithms presented here give the same solution as the 2D algorithm and pre-

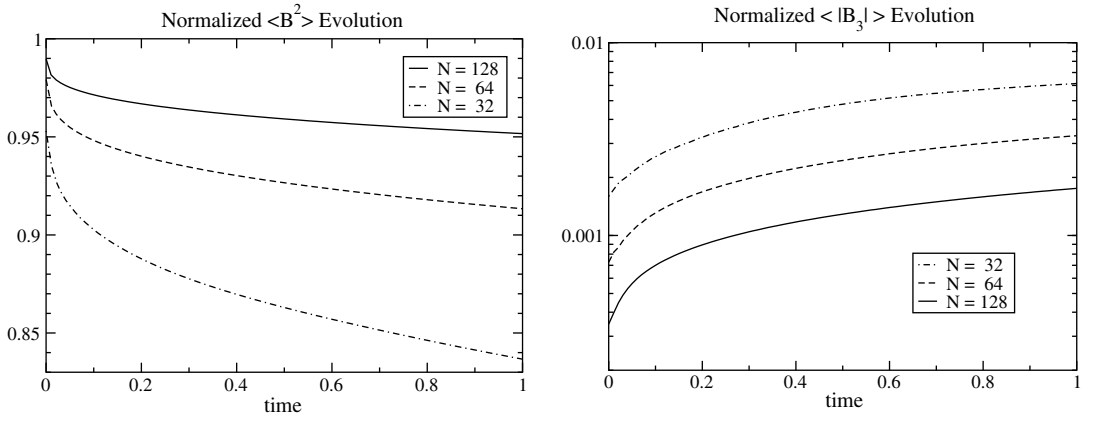

Fig. 1. Time evolution of the normalized, volume average magnetic energy density $\langle B^2 \rangle$ and the component along the x_3-direction, $\langle B_3^2 \rangle$, for three different grid resolutions using the 6-solve integration algorithm.

serve the solution $B_z = 0$ for all time (we have explicitly tested that this is true with our implementation of the method). With the axis of the cylindrical field loop is aligned along a non-special direction with respect to the grid, preserving this property is non-trivial.

As a quantitative measure of the ability of the algorithm to preserve $B_3 = 0$ we plot the normalized error $\langle |B_3| \rangle / B_0$ in Fig. 1. This error is calculated by contracting the cell center magnetic field with a unit vector in the x_3-direction and computing the volume average of its absolute value. From this plot it is clear that the convergence rate of $\langle |B_3| \rangle / B_0$ as measured in either the initial conditions, or the solution at time = 1 is approximately first order. This behavior is consistent with the observation that the 3-component of the magnetic energy is dominant on the axis and at the boundary of the magnetic cylinder where the current density is initially singular, as shown in Fig. 2. It is also worth noting that away from these regions, the solution preserves the 3-component of the magnetic energy quite small. This would not be the case if care were not taken to balance the MHD source terms in the integration algorithm.

5.2. Linear wave convergence

Convergence of the errors in the propagation of linear amplitude, planar waves in a direction which is oblique to the grid provides a quantitative test of both the 6-solve and 12-solve CTU-CT MHD algorithms. The problem is most easily described in a coordinate system (x_1, x_2, x_3) which is chosen such that the wave propagates parallel to the x_1-axis. In this coordinate system, the initial conserved variable state vector is given by

$$q^0 = \bar{q} + \varepsilon R_p \cos\left(\frac{2\pi x_1}{\lambda}\right), \tag{53}$$

where $\bar{q}$ is the mean background state, $\varepsilon = 10^{-6}$ is the wave amplitude, and R_p is the right eigenvector in conserved variables for wave mode p (calculated in the state $\bar{q}$). In order to enable others to perform the same tests presented here and compare the results in a quantitative manner, we include the numerical values for the right eigenvectors in the Appendix.

The mean background state $\bar{q}$ is selected so that the wave speeds are well separated and there are no inherent symmetries in the magnetic field orientation (when initialized on the grid). The density $\bar{\rho} = 1$ and gas pressure $\bar{P} = 1/\gamma = 3/5$. The velocity component $\bar{v}_1 = 1$ for the entropy mode test and $\bar{v}_1 = 0$ for all other wave modes. The transverse velocity components $\bar{v}_2 = \bar{v}_3 = 0$. The magnetic field components $\bar{B}_1 = 1$, $\bar{B}_2 = 3/2$, and $\bar{B}_3 = 0$. With this choice, the slow-mode speed $c_s = 1/2$, the Alfvén speed $c_a = 1$, and the fast mode speed $c_f = 2$ in the x_1-direction.

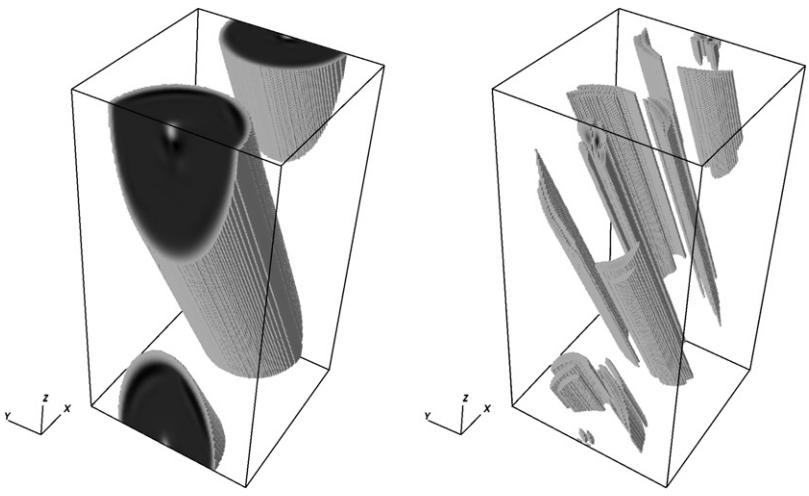

Fig. 2. Thresholded image of the magnetic energy (left) and the 3-component of the magnetic energy, $B_3^2/2$, at time = 1.

The computational domain extends from $0 \leqslant x \leqslant 3.0$, $0 \leqslant y \leqslant 1.5$, and $0 \leqslant z \leqslant 1.5$, is resolved on a $2N \times N \times N$ grid and uses periodic boundary conditions. Initializing this problem on the computational grid is accomplished by applying a coordinate transformation

$$\begin{aligned} x &= x_1 \cos\alpha \cos\beta - x_2 \sin\beta - x_3 \sin\alpha \cos\beta, \\ y &= x_1 \cos\alpha \sin\beta + x_2 \cos\beta - x_3 \sin\alpha \sin\beta, \\ z &= x_1 \sin\alpha + x_3 \cos\alpha \end{aligned} \tag{54}$$

from the (x_1, x_2, x_3) coordinate system to the (x, y, z) coordinate system of the grid with $\sin\alpha = 2/3$ and $\sin\beta = 2/\sqrt{5}$. With this choice, there is one wave period along each grid direction and the wavelength $\lambda = 1$. The interface components of the magnetic field are initialized via a magnetic vector potential so as to ensure $\nabla \cdot \mathbf{B} = 0$.

The error in the solution is calculated after propagating the wave for a distance equal to one wavelength at a time $t = \lambda/c$ where c is the speed of the wave mode under consideration. For each component s of the conserved variable vector q we calculate the L1-error with respect to the initial conditions

$$\delta q_s = \frac{1}{2N^3} \sum_{i,j,k} |q^n_{i,j,k,s} - q^0_{i,j,k,s}| \tag{55}$$

by summing over all grid cells (i, j, k). We use the cell center components of the magnetic field in computing this error. In Fig. 3, we plot the norm of this error vector

$$\|\delta q\| = \sqrt{\sum_s (\delta q_s)^2} \tag{56}$$

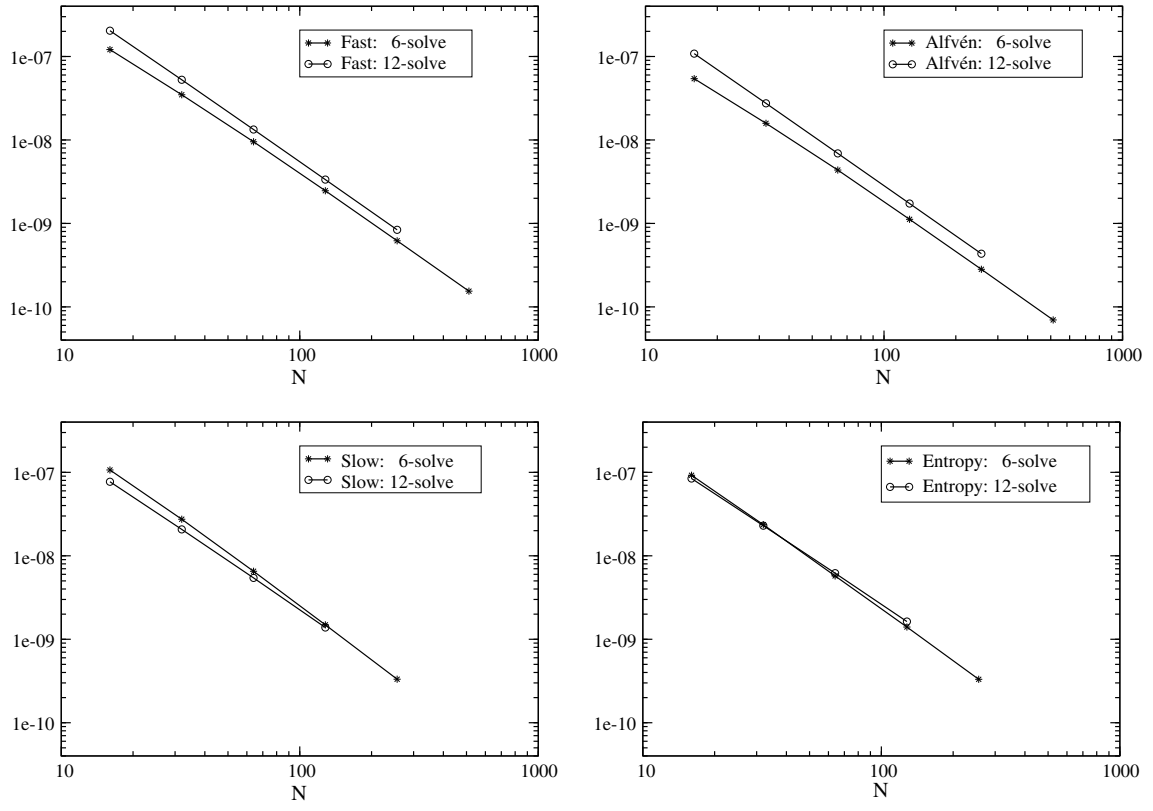

Fig. 3. Linear wave convergence of fast, Alfvén, slow and entropy modes using the CTU + CT 6-solve and 12-solve integration algorithms. The symbols denote the calculated L1-error norm.

for the fast, Alfvén, slow and entropy modes. Both algorithms demonstrate a second-order convergence. With the exception of the slow mode, the 6-solve algorithm shows lower errors than the 12-solve algorithm. Note that the choice of maximum resolution in the convergence study for each algorithm and wave mode was selected on the basis of the "cost" of the computation.

5.3. Circularly polarized Alfvén wave

The propagation of a circularly polarized Alfvén wave in a periodic domain provides another quantitative test since such waves are an exact nonlinear solution to the ideal MHD equations [19]. Although for some parameters circularly polarized Alfvén waves are susceptible to a parametric instability [12,10], for the parameters used here, [19], we find no indication of instability.

As with the linear wave propagation study presented in Section 5.2, the initial conditions are most easily described in a coordinate system (x_1, x_2, x_3) which is chosen such that the wave propagates parallel to the x_1-axis. In this coordinate system, the magnetic field components $B_1 = 1, B_2 = 0.1\sin(2\pi x_1/\lambda)$, and $B_3 = 0.1\cos(2\pi x_1/\lambda)$. The velocity components $v_1 = (0, 1)$ for traveling or standing Alfvén waves, respectively, $v_2 = 0.1\sin(2\pi x_1/\lambda)$, and $v_3 = 0.1\cos(2\pi x_1/\lambda)$. The mass density $\rho = 1$ and the gas pressure $P = 0.1$, hence $\beta = 2P/B^2 \sim 0.2$.

The computational domain is identical to that used in Section 5.2. We use the coordinate transformation given by Eq. (54) and a magnetic vector potential to initialize the magnetic fields so as to ensure $\mathbf{\nabla}\cdot\mathbf{B} = 0$. It is worth noting that this approach will necessarily result in magnetic pressure perturbations as a result of truncation error in initializing the magnetic field on the grid. Since $B_\perp^2/P = 0.1$ this truncation error in initialization will drive compressive waves. Note that with this set of initial conditions and $v_1 = 0$ the Alfvén wave will travel a distance of one wavelength λ in a time $t = 1$.

As a quantitative measure of the solution accuracy, we present in Fig. 4 the norm of the L1-error vector (as defined in Eq. (56)) after propagating for a time $t = 1$ for both standing and traveling wave modes. From this figure, we see that both traveling and standing circularly polarized Alfvén waves converge with second-order accuracy for both integration algorithms. The traveling wave mode shows a larger error amplitude relative to the standing mode, but it is worth noting that (while not shown here) the increase is fairly uniform over the components of the error vector. The 6-solve and 12-solve algorithms show quite comparable errors for both standing and traveling wave modes. When using a CFL number of 0.4, the 12-solve and 6-solve algorithms result in nearly identical errors. Increasing the CFL number to 0.8 with the 12-solve algorithm results in a slightly reduced traveling wave error, and increased standing wave error. These results indicate that the dominant difference in the L1-error between the 6-solve and 12-solve algorithms results from the CFL dependence of the truncation error.

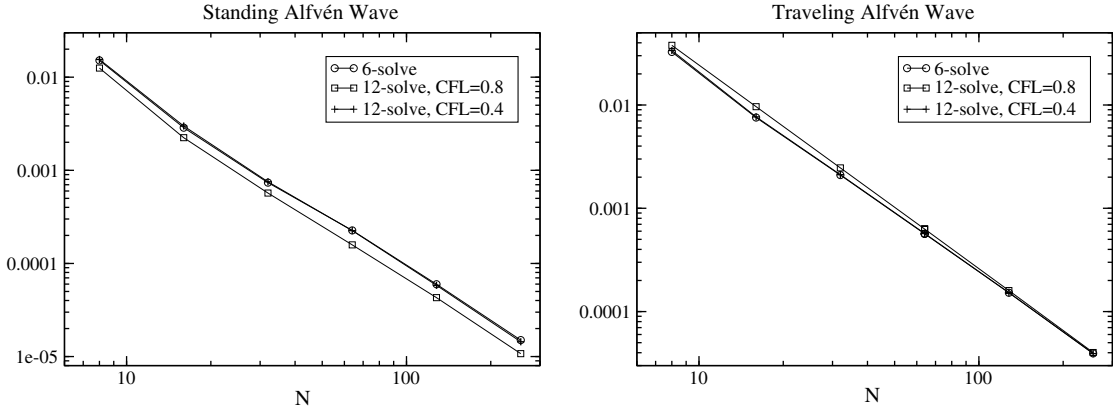

Fig. 4. L1-error norm for the 6-solve and 12-solve integration algorithms for both standing (left) and traveling (right) circularly polarized Alfvén waves. In particular note the dominant difference between the 12-solve and 6-solve errors is attributable to the CFL dependence.

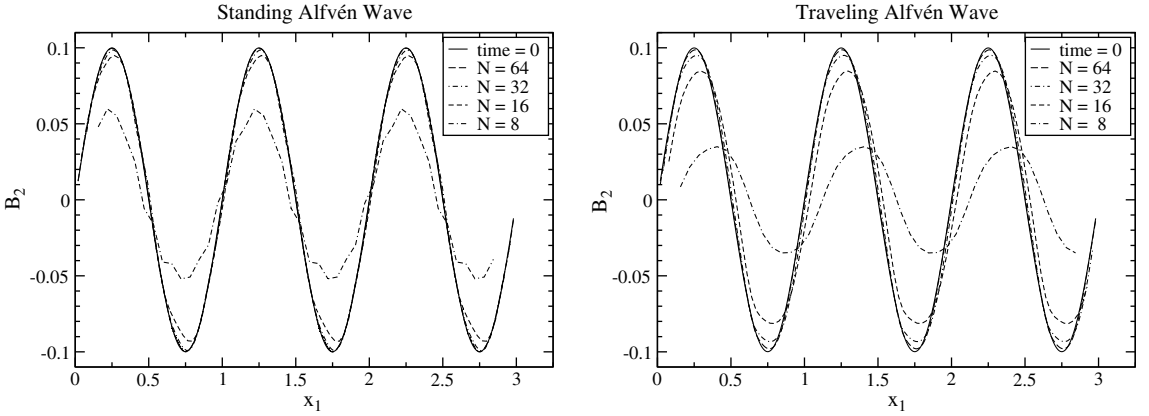

Fig. 5. Plot of B_2 versus x_1 at $t = 5$ for the standing (left) and traveling (right) circularly polarized Alfvén waves using the 6-solve integration algorithm. For comparison, the initial conditions at $t = 0$ for the $N = 64$ case is also included.

As a qualitative measure of the solution accuracy, we present in Fig. 5 scatter plots of B_2 versus x_1 for both standing and traveling wave modes after propagating for a time $t = 5$ using the 6-solve integration algorithm. These plots are constructed using the cell center components of the magnetic field, the cell center position and the coordinate transformation given by Eq. (54). As a result of the fact that the wave is rotated with respect to the grid, there are many grid cells with the same cell center x_1-position. Hence, since these plots include every grid point in the grid, the lack of scatter in the plots demonstrates that the Alfvén waves retain their planar symmetry throughout the calculation. Unfortunately, it is difficult to use the results presented here to make direct contact with solutions presented in the literature due to the scarcity of published 3D test solutions. For analogous plots in a 2D system see [19,15,1].

As a final measure of the solution accuracy and convergence, we present results for the dissipation of magnetic helicity in the case of a traveling circularly polarized Alfvén wave. We note that this is not the cleanest possible *test*, since with periodic boundary conditions and a mean magnetic field, it does not appear to be generally possible to define a magnetic helicity which is conserved [5]. Nevertheless, we find that following [4] the magnetic helicity evolution associated with the fluctuating components of the magnetic field gives an interesting constraint on the problem considered here. In particular, let $\mathbf{B}_0 = \langle \mathbf{B} \rangle$ (where angle brackets denote a spatial mean) and $\mathbf{b} = \mathbf{B} - \mathbf{B}_0$ denote the mean and fluctuating components of the magnetic field, respectively. Also, define the magnetic vector potential associated with the fluctuating field as $\mathbf{b} = \nabla \times \mathbf{a}$. It is worth noting that as a result of periodic boundary conditions, $\mathbf{B}_0$ is time independent and the magnetic helicity associated with the fluctuating field $H = \langle \mathbf{b} \cdot \mathbf{a} \rangle$ is gauge invariant. It follows that the time evolution of the magnetic helicity is given by

$$\frac{\mathrm{d}}{\mathrm{d}t}\langle \mathbf{b} \cdot \mathbf{a} \rangle = -2\langle \mathbf{E} \cdot \mathbf{b} \rangle, \tag{57}$$

where $\mathbf{E}$ is the electric field. Assuming ideal MHD, this equation can also be written as

$$\frac{\mathrm{d}}{\mathrm{d}t}\langle \mathbf{b} \cdot \mathbf{a} \rangle = -2\mathbf{B}_0 \cdot \langle \mathbf{v} \times \mathbf{b} \rangle. \tag{58}$$

From this expression it is clear for a circularly polarized Alfvén wave the magnetic helicity should be conserved with $\langle \mathbf{b} \cdot \mathbf{a} \rangle = B_\perp^2/k$.

In Fig. 6, we present the time evolution of the normalized magnetic helicity $\widetilde{H} = (k/B_\perp^2)\langle \mathbf{b} \cdot \mathbf{a} \rangle$ for a traveling Alfvén wave using the 6-solve integration algorithm for a variety of resolutions. The plots in this figure show two basic phenomena, dissipation and weak oscillations. The oscillations are an indication that the circularly polarized Alfvén wave is not resolved exactly. Certain features regarding the oscillations are worth mentioning. First, the oscillation period $\tau = 1/2$ independent of the grid resolution and whether the Alfvén wave is standing or traveling with respect to the grid. Second, the amplitude of the oscillations in the helicity

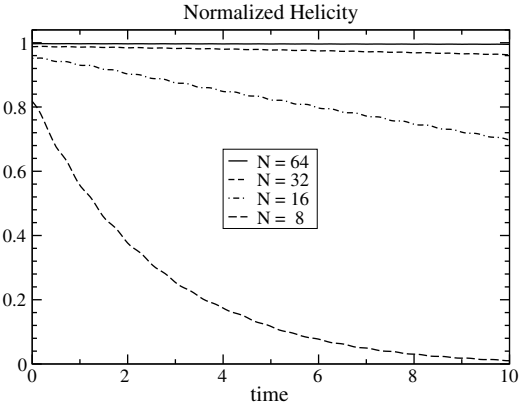

Fig. 6. Plot of the normalized magnetic helicity $\widetilde{H} = (k/B_\perp^2)\langle \mathbf{b} \cdot \mathbf{a} \rangle$ as a function of time for different resolutions.

varies with resolution proportional to N^{-2}. Third, the oscillations are consistent in both amplitude and phase with the independently measured volume average quantity $\mathbf{B}_0 \cdot \langle \mathbf{v} \times \mathbf{b} \rangle$. These details support the conclusion that the oscillations are a result of truncation error in resolving the wave.

5.4. MHD Riemann problem inclined to the grid

The Riemann problem is a favorite test for numerical algorithms since it can be chosen to study smooth flows, discontinuous flows, or a combination thereof. To make the test multidimensional, the normal direction of the initial interface is chosen such that it has no special orientation with respect to the computational grid. In this configuration it provides a measure of the ability of the computational algorithm to faithfully reproduce the 1D solution on the large scale, despite the fact that on the scale of grid cells the flow contains multidimensional, interacting waves.

We begin by choosing a coordinate system (x_1, x_2, x_3) with the Riemann problem interface located at $x_1 = 0$ and will use the terms left and right states to refer to the regions $x_1 < 0$ and $x_1 > 0$, respectively. To map the initial conditions to the computational domain, we apply the coordinate transformation in Eq. (54) with the choice of rotation angles described below. This coordinate transformation can be inverted to read

$$\begin{aligned} x_1 &= x\cos\alpha\cos\beta + y\cos\alpha\sin\beta + z\sin\alpha, \\ x_2 &= -x\sin\beta + y\cos\beta, \\ x_3 &= -x\sin\alpha\cos\beta - y\sin\alpha\sin\beta + z\cos\alpha. \end{aligned} \tag{59}$$

Using the fact that the initial conditions and solution to the Riemann problem are a function of the x_1-coordinate alone, the solution vector $q(\mathbf{x} + \mathbf{s}) = q(\mathbf{x})$ for a translation vector $\mathbf{s}$ which satisfies $x_1(\mathbf{x} + \mathbf{s}) = x_1(\mathbf{x})$. Making use of Eq. (59) we find that the continuous set of translation vectors $\mathbf{s}$, for which the solution is invariant, satisfies the equation

$$s_x\cos\alpha\cos\beta + s_y\cos\alpha\sin\beta + s_z\sin\alpha = 0. \tag{60}$$

For the problem at hand we are interested in the discrete set of translation vectors for which $(s_x, s_y, s_z) = (n_x\delta x, n_y\delta y, n_z\delta z)$ where (n_x, n_y, n_z) are integers and $(\delta x, \delta y, \delta z)$ are the grid cell size in each direction. Making this substitution, and rearranging terms we find

$$n_x + n_y\frac{\delta y}{\delta x}\tan\beta + n_z\frac{\delta z\tan\alpha}{\delta x\cos\beta} = 0. \tag{61}$$

We next choose the rotation angles (α, β) such that

$$\frac{\delta y}{\delta x}\tan\beta = \frac{r_x}{r_y} \quad \text{and} \quad \frac{\delta z\tan\alpha}{\delta x\cos\beta} = \frac{r_x}{r_z}, \tag{62}$$

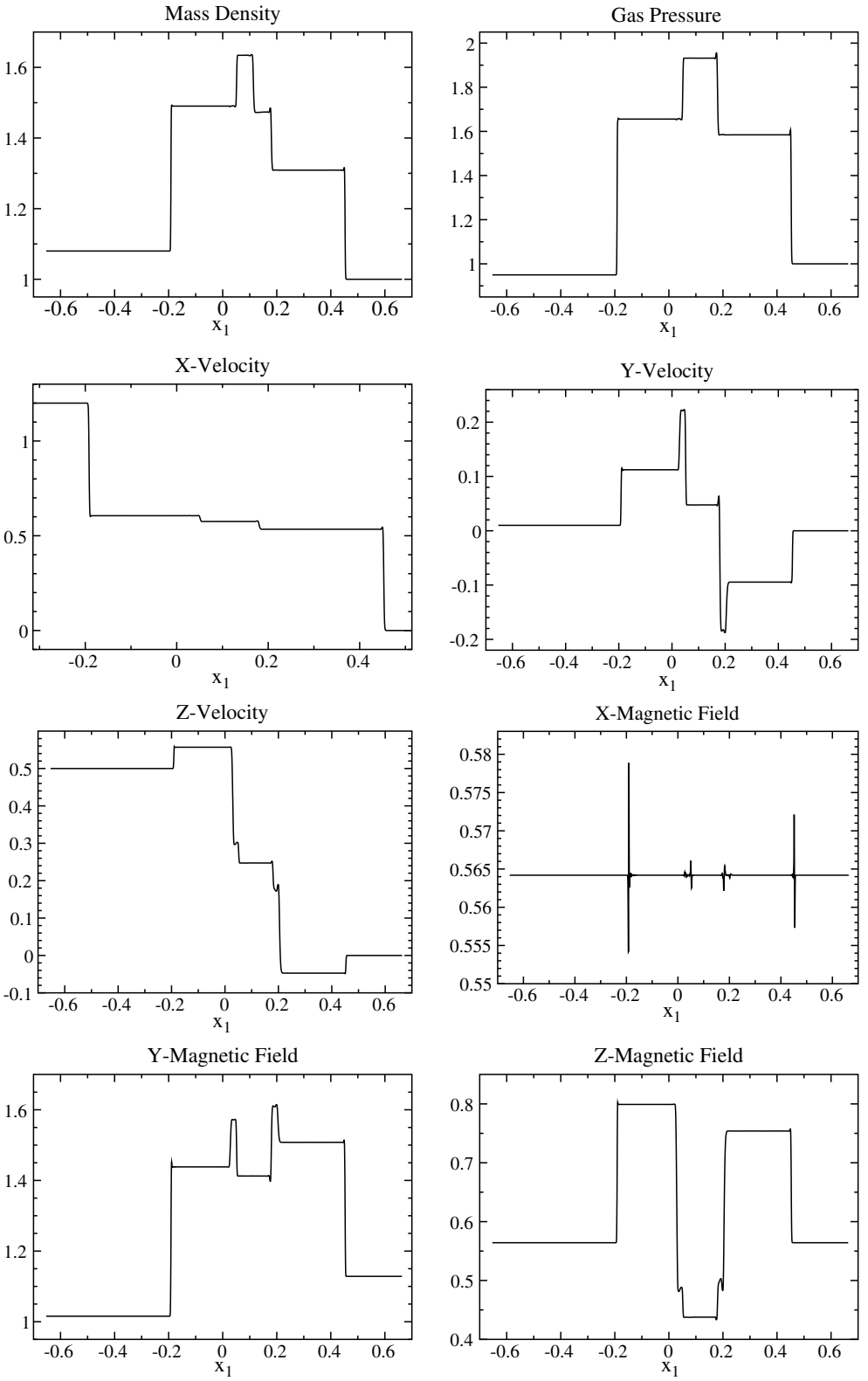

Fig. 7. Solution to the Riemann problem in a direction oblique to the grid.

where (r_x, r_y, r_z) are integers. With this choice, our equation for translation invariance becomes

$$\frac{n_x}{r_x} + \frac{n_y}{r_y} + \frac{n_z}{r_z} = 0. \tag{63}$$

Note that the translation invariance described by Eq. (63) was constructed by considering a point translation symmetry and as such applies equally well to volume and interface averaged quantities. That is, there are no approximations involved in the statement that $q_{i,j,k} = q_{i+n_x,j+n_y,k+n_z}$ for (n_x, n_y, n_z) which satisfy (63). Also note that one coordinate direction, say the x-direction, can be isolated as the principle simulation direction and the transverse directions can be made as small as (r_y, r_z). Finally, note that the translation invariance relation (63) is the key relation for mapping computational grid cells to ghost cells for imposing boundary conditions.

The specific Riemann problem we consider in this section is presented in [16] in test problem 2a. In the (x_1, x_2, x_3) coordinate system, the left state is initialized with $\rho = 1.08$, $(v_1, v_2, v_3) = (1.2, 0.01, 0.5)$, $(B_1, B_2, B_3) = (2/\sqrt{4\pi}, 3.6/\sqrt{4\pi}, 2/\sqrt{4\pi})$ and $P = 0.95$. The right state is initialized with $\rho = 1.0, (v_1, v_2, v_3) = (0, 0, 0), (B_1, B_2, B_3) = (2/\sqrt{4\pi}, 4/\sqrt{4\pi}, 2/\sqrt{4\pi})$ and $P = 0.95$. This problem is then mapped to the 3D domain with the rotation parameters $(r_x, r_y, r_z) = (1, 2, 4)$. The computational grid has $(N_x, N_y, N_z) = (768, 8, 8)$ grid cells covering the domain $-0.75 \leqslant x \leqslant 0.75, 0 \leqslant y \leqslant 1/64, 0 \leqslant z \leqslant 1/64$ and hence has a resolution of $\delta x = \delta y = \delta z = 1/512$.

The solution at time $= 0.2$ is presented in Fig. 7 using the 6-solve CTU algorithm. These plots include the cell-center data from every grid cell using the coordinate transformation in Eq. (54). Note in these plots is that since $N_y > r_y$ and $N_z > r_z$ there are multiple grid cells with the same cell-center x_1-position. Therefore, the lack of scatter in these plots indicates that the algorithm retains the planar symmetry throughout the simulation. A comparison of the results presented here to the 1D solution using the underlying PPM algorithm, with the same resolution, i.e. $\delta x = 1/512$, indicates that the 3D solution has dissipation characteristics which are nearly identical to the 1D algorithm. The dominant difference between the 1D and 3D solutions is the presence of oscillations at the slow, Alfvén and fast mode discontinuities.

One question which has received a good deal of attention with this class of problem is the ability of the computational algorithm to maintain the parallel component of the magnetic field, B_1, equal to a constant. It is important to point out that oscillations are likely unavoidable unless the orientation of the Riemann problem is chosen to be aligned in a special direction with respect to the grid. As evidence of this fact, we note that the in the initial conditions, the cell-center B_1-component of the magnetic field shows an oscillation with an amplitude of approximately 8.26×10^{-3} despite the fact that the interface averaged magnetic fields were initialized with an "exact" integral average using a magnetic vector potential. This oscillation is therefore a result of the discretization relating the cell-center and interface averaged magnetic field components. In the initial conditions, as well as the solution at time $= 0.2$, the oscillations in B_1 occur wherever the transverse components of the magnetic field rotate over a small scale such as the initial discontinuity, and the resultant fast, Alfvén and slow mode discontinuities. Finally, we note that just as in the 2D paper [1], the oscillations in the parallel component of the magnetic field can be eliminated by restricting the solution to "macrocells". This operation effectively aligns the x_1-direction with the macrocell $[1, 1, 1]$ direction.

5.5. MHD blast wave

Our final test problem is the explosion of a centrally over pressurized region into a low pressure, low β ambient medium. This test combines shocked flows, smooth flow regions, and strong magnetic fields. While the results are not particularly quantitative in their measure of the accuracy, this test is a good measure of the robustness of the integration algorithm. Variants on this problem have been presented by a number of authors [20,3,13,1] and here we choose to use the parameters given by [13] for a 3D domain.

The computational domain extends from $-0.5 \leqslant x \leqslant 0.5$, $-0.5 \leqslant y \leqslant 0.5$ and $-0.5 \leqslant z \leqslant 0.5$. The density $\rho = 1$, the velocity $\mathbf{v} = \mathbf{0}$, and the magnetic field components $B_x = B_z = 10/\sqrt{2}$ and $B_y = 0$. Within a sphere of radius $R = 0.125$ about the origin the gas pressure $P = 100$ and $\beta = 2P/B^2 = 2$. Outside of this sphere, the gas pressure $P = 1$ and $\beta = 2 \times 10^{-2}$. These initial conditions are evolved until a time $t = 0.02$ using a 200^3 computational grid.

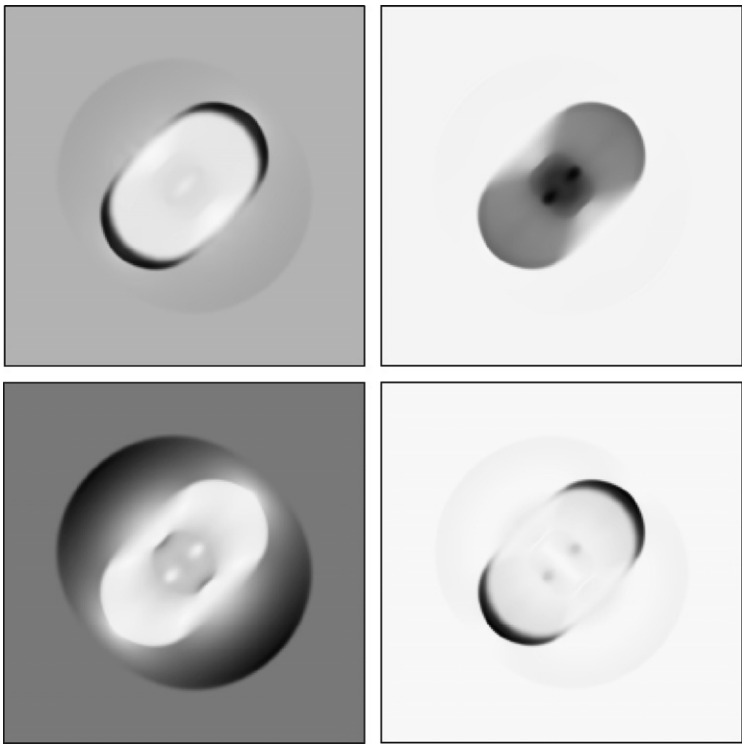

Fig. 8. Linearly scaled grey-scale images of the evolved state (time = 0.02) for the MHD blast wave problem. The density (top left) ranges from 0.190 (white) to 2.98 (black). The gas pressure (top right) ranges from 1.0 (white) to 42.4 (black). The magnetic energy density (bottom left) ranges from 25.2 (white) to 64.9 (black). The kinetic energy density (bottom right) ranges from 0.0 (white) to 33.1 (black).

In Fig. 8, we present images of the density, pressure, magnetic and kinetic energy density sliced along the $y = 0$ plane at the end time. The general structure of the solution is the same as one finds in the 2D calculation. Namely, the outermost surface in this expanding shell is a fast-shock which is only weakly compressive and energetically is dominated by the magnetic field. Interior to this, one finds two dense shells of gas which propagate parallel to the magnetic field. These shells are bounded by a slow-mode shock and contact surface (separating the initially hot, interior gas from the surrounding cool ambient medium) on the outer and inner surfaces, respectively. The maximum compression of the ambient gas by the slow-mode shock is approximately 3.3, the same as was found in the 2D calculation. The fact that the 2D and 3D calculations show quantitatively similar compression in the slow-mode shock is an indication that their motion is approximately 1D, i.e. parallel to the magnetic field.

These results demonstrate that the 6-solve integration algorithm is a robust algorithm, capable of evolving shocked flows with $\beta \sim 10^{-2}$. Moreover, since the integration algorithm is unsplit, it preserves the symmetry of the initial conditions naturally.

6. Conclusion

In this paper, we have presented an algorithm for 3D MHD which combines the (6-solve) corner transport upwind integration algorithm with the method of constrained transport for evolving the magnetic field. This algorithm is a natural extension, and generalization of the 2D algorithm [1]. In addition, we have outlined the essential elements to constructing a 12-solve CTU with CT integration algorithm for MHD and included results of this algorithm in Section 5. Both the 6-solve and 12-solve algorithms are found to be accurate and robust for approximately the same computational cost. As a result, we generally prefer the 6-solve algorithm as a result of its simplicity and smaller memory footprint.

The 3D MHD PPM interface states algorithm presented in this paper is a new and essential element of the integration algorithms. We have shown here that this is a natural extension of the 2D MHD PPM interface states algorithm presented in [1] and that it reduces identically to the 2D algorithm in the grid-aligned, plane-parallel limit. The 3D MHD PPM interface states algorithm was designed in such a way as to satisfy a multidimensional balance law involving what we have referred to here as MHD source terms. Failure to satisfy this balance law is found to result in erroneous and secular evolution of the magnetic field under quite general conditions, e.g. the advection of a high β magnetic field loop.

We have also presented a variety of test results for both the 6- and 12-solve MHD CTU CT integration algorithms. These test problems were selected so as to enable a comparison with previously published results, as well as to introduce new, quantitative measures of the solution accuracy. One interesting result of these tests is the observation that the dominant difference in the L1-error for the 6- and 12-solve algorithm convergence on smooth wave propagation is attributable to the CFL number dependence. Throughout this section we have included the necessary information so as to enable other researchers involved in developing or applying MHD algorithms to make a quantitative, as well as qualitative, comparison with the results in this paper.

Finally, it is worth noting that the integration algorithms presented here have been thoroughly tested on a great many test problems not included here. These include problems which are also of interest for their scientific merit. Examples include a study of the magneto-rotational instability [2] and the MHD Raleigh Taylor instability [18]. In a future paper, we will detail our approach to combining the integration algorithms presented here with the methods of static and adaptive mesh refinement.

Acknowledgments

Simulations were performed on the Sun Grid computational facility, Teragrid cluster at NCSA, the IBM Blue Gene at Princeton University, and on computational facilities supported by NSF Grant AST-0216105. Financial support from DoE Grant DE-FG52-06NA26217 is acknowledged.

Appendix A. Linear wave right eigenvectors

In order to enable others to perform the linear wave convergence test presented in Section 5.2 and compare their results in a quantitative manner, we include the numerical values for the right eigenvectors here. In the wave-aligned coordinate system (x_1, x_2, x_3) the conserved variable vector and right eigenvectors (labeled according to their propagation velocity) are given by

$$q = \begin{pmatrix} \rho \\ \rho v_1 \\ \rho v_2 \\ \rho v_3 \\ B_1 \\ B_2 \\ B_3 \\ E \end{pmatrix}, \quad R_{\pm c_f} = \frac{1}{2\sqrt{5}} \begin{pmatrix} 2 \\ \pm 4 \\ \mp 2 \\ 0 \\ 0 \\ 4 \\ 0 \\ 9 \end{pmatrix}, \quad R_{\pm c_a} = \begin{pmatrix} 0 \\ 0 \\ 0 \\ \mp 1 \\ 0 \\ 0 \\ 1 \\ 0 \end{pmatrix}, \quad R_{\pm c_s} = \frac{1}{2\sqrt{5}} \begin{pmatrix} 4 \\ \pm 2 \\ \pm 4 \\ 0 \\ 0 \\ -2 \\ 0 \\ 3 \end{pmatrix}, \quad R_{v_1} = \frac{1}{2} \begin{pmatrix} 2 \\ 2 \\ 0 \\ 0 \\ 0 \\ 0 \\ 0 \\ 1 \end{pmatrix}. \tag{A.1}$$

References

[1] T.A. Gardiner, J.M. Stone, An unsplit Godunov method for ideal MHD via constrained transport, J. Comput. Phys. 205 (2005) 509.
[2] S.A. Balbus, J.F. Hawley, Instability, turbulence, and enhanced transport in accretion disks, Rev. Mod. Phys. 70 (1998) 1.
[3] D.S. Balsara, D.S. Spicer, A staggered mesh algorithm using high order Godunov fluxes to ensure solenoidal magnetic fields in magnetohydrodynamic simulations, J. Comput. Phys. 149 (1999) 270.
[4] A. Brandenburg, W.H. Matthaeus, Magnetic helicity evolution in a periodic domain with imposed field, Phys. Rev. E 69 (2004) 056407.
[5] M.A. Berger, Magnetic helicity in a periodic domain, J. Geophys. Res. 102 (1997) 2637.

[6] J.U. Brackbill, D.C. Barnes, The effect of nonzero $\nabla \cdot B$ on the numerical solution of the magnetohydrodynamic equations, J. Comput. Phys. 35 (1980) 426.
[7] P. Colella, Multidimensional upwind methods for hyperbolic conservation laws, J. Comput. Phys. 87 (1990) 171.
[8] P. Colella, P.R. Woodward, The piecewise parabolic method (PPM) for gas-dynamical simulations, J. Comput. Phys. 54 (1984) 174.
[9] R.K. Crockett, P. Colella, R.T. Fisher, R.I. Klein, C.F. McKee, An unsplit, cell-centered Godunov method for ideal MHD, J. Comput. Phys. 203 (2005) 422.
[10] L. Del Zanna, M. Velli, P. Londrillo, Parametric decay of circularly polarized Alfvén waves: multidimensional simulations in periodic and open domains, Astron. Astrophys. 367 (2001) 705.
[11] C.R. Evans, J.F. Hawley, Simulation of magnetohydrodynamic flows: a constrained transport method, Astrophys. J. 322 (1988) 659.
[12] M.L. Goldstein, An instability of finite amplitude circularly polarized Alfvén waves, Astrophys. J. 219 (1978) 700.
[13] P. Londrillo, L. Del Zanna, High-order upwind schemes for multidimensional magnetohydrodynamics, Astrophys. J. 530 (2000) 508.
[14] G.H. Miller, P. Colella, A conservative three-dimensional Eulerian method for coupled solid-fluid shock capturing, J. Comput. Phys. 183 (2002) 26.
[15] U. Pen, P. Arras, S. Wong, A free, fast, simple and efficient TVD MHD code, Astrophys. J. Suppl. 149 (2003) 447.
[16] D. Ryu, T.W. Jones, Numerical magnetohydrodynamics in astrophysics: algorithm and tests for one-dimensional flow, Astrophys. J. 442 (1995) 228.
[17] J. Saltzman, An unsplit 3D upwind method for hyperbolic conservation laws, J. Comput. Phys. 115 (1994) 153.
[18] J.M. Stone, T.A. Gardiner, Nonlinear evolution of the magnetohydrodynamic Rayleigh–Taylor instability, Phys. Fluids 19 (2007) 094104.
[19] G. Tóth, The $\nabla \cdot B = 0$ constraint in shock-capturing magnetohydrodynamics codes, J. Comput. Phys. 161 (2000) 605.
[20] A.L. Zachary, A. Malagoli, P. Colella, A higher-order Godunov method for multidimensional ideal magnetohydrodynamics, SIAM J. Sci. Comput. 15 (1994) 263.